

Cathode Processing Optimization Toward Solid-State Batteries with Monolithic Oxsulfide Glassy Solid Electrolytes

Will Fettkether, Jacob Wheaton, Nicholas H. Bashian, and Steve W. Martin*

Seeking to further the development of all-solid-state lithium-ion batteries (ASSLIBs), an optimized composite cathode blend for lithium-ion batteries (LIBs) is fabricated via planetary ball mill using LiFePO₄, a mixed oxsulfide (MOS) glassy solid electrolyte (GSE), called LiSiPSO, a carbon additive, and styrene-butadiene rubber binder. The ionic and electronic conductivities of the composite cathode are evaluated using electrochemical impedance spectroscopy (EIS). Using EIS measurements, the milling time and processing order of forming the composite mixture are modified to improve these transport properties. By tailoring

the processing methods used to create the composite cathode, ASSLIBs fabricated with optimized cathodes in conjunction with a monolithic GSE display good specific capacities (100 mAh g⁻¹ initial) and coulombic efficiencies (>95%) at room temperature, demonstrating the viability of monolithic MOS GSEs in ASSLIBs. Cyclic voltammetry, galvanostatic cycling with potential limits, and postmortem Raman spectroscopy reveal an irreversible reaction and growing instability within the cycled cells, meriting further research to produce LIBs with higher capacities and longer cycle lives through the development of more stable GSEs.

1. Introduction

With the increasing prevalence of electric vehicles and renewable energy generation, the demand for batteries with higher energy densities, longer cycle lives, and increased safety has grown rapidly.^[1,2] While modern lithium-ion battery (LIB) technology has been established since 1991, solid-state battery approaches utilizing lithium metal anodes promise higher energy density and longer cycle life. Solid-state electrolytes (SSEs) are key to enabling lithium metal anodes by counteracting the instability and associated safety concerns of traditional organic liquid electrolytes in contact with lithium metal.^[3,4]

Intrinsically, SSEs must possess a high ionic conductivity ($\geq 10^{-3}$ [$\Omega \cdot \text{cm}$]⁻¹), low electronic conductivity ($< 10^{-9}$ [$\Omega \cdot \text{cm}$]⁻¹), and be electrochemically stable from 0 to 5 V versus Li/Li⁺ to allow for usage with high voltage cathodes.^[5–7] High ionic conductivity allows for lower internal resistances, and therefore, lower overpotentials, while a low electronic conductivity inhibits parasitic charge losses and dendrite formation.^[8] To prevent poor cycling behavior and low coulombic efficiency due to side reactions, the SSE should be electrochemically stable in the operating voltage window of 0–5 V versus Li/Li⁺.^[9]

To create battery systems that meet these requirements, this work has focused on the use of inorganic, mixed oxsulfide (MOS) glasses as the SSE in LIBs. Glassy solid electrolytes (GSEs) have several advantageous properties compared to other classes of SSEs. They often possess higher ionic conductivities than their crystalline counterparts, and the absence of grain boundaries inhibits dendrite formation.^[10,11] MOS GSEs meet many of the intrinsic requirements necessary for an SSE: high ionic conductivity, low electronic conductivity, and good electrochemical stability.^[12–15] Additionally, MOS GSEs meet the physicochemical requirements necessary to facilitate highly scalable mass production.^[16,17] The viscoelastic behavior and excellent thermal properties of MOS GSEs are conducive to good manufacturability, as GSEs can be formed via low-cost, scalable methods, such as film-redrawing.^[13,18,19] Many laboratory demonstrations of all solid-state batteries (ASSBs) rely on powdered GSE compacted at high pressures and cycled at stack pressures unfeasible for commercial cells.^[20] One method of overcoming these production challenges is to use a monolithic GSE manufactured via film-redraw that can be cycled at low stack pressures (< 1 MPa) with appreciable capacities. Such a battery configuration would be better suited to scaling toward mass production.

Despite their advantages, monolithic GSEs also present certain challenges for use as SSEs in ASSBs. As with most inorganic SSEs, the high resistivity of the solid–solid interfaces between the cathode and electrolyte inhibits charge transport.^[6,17] Thus, in order to create an effective cell, it is important to optimize the ionic and electronic conductivities of the cathode materials used in contact with the GSE and within the cathode itself.^[21] To accomplish this goal, composite cathodes are used, which utilize various materials to enable Li⁺ transport and storage. The components chosen must be electrochemically stable in contact with each other and possess sufficient conductivities for both ionic

W. Fettkether, J. Wheaton, N. H. Bashian, S. W. Martin

Department of Materials Science & Engineering
Iowa State University of Science & Technology
Ames 50010–1096, Iowa, USA
E-mail: swmartin@iastate.edu

 Supporting information for this article is available on the WWW under <https://doi.org/10.1002/batt.202500065>

 © 2025 The Author(s). *Batteries & Supercaps* published by Wiley-VCH GmbH. This is an open access article under the terms of the Creative Commons Attribution License, which permits use, distribution and reproduction in any medium, provided the original work is properly cited.

and electronic charge transfer. These challenges must be resolved simultaneously to achieve good cathode performance.

Toward these ends, this work has investigated the optimization conditions to create composite cathodes for use in conjunction with a monolithic MOS GSE. The novel blend consists of carbon-coated LiFePO₄ (LFP) as the cathode active material (CAM), a milled GSE for ionic conduction, carbon nanotubes to support high electronic conduction, and styrene-butadiene rubber (SBR) as a binder. LFP was selected due to its relatively low cost and the abundance of investigations in literature as an intercalation cathode.^[22,23] The processing conditions of this composite cathode were optimized to achieve higher ionic and electronic conductivities. Both component mixing orders and processing times were systematically varied to optimize ionic and electronic conductivity in tape-cast cathodes, and the interface between the cathode and monolithic MOS GSE was mediated by the addition of a small amount of solvate ionic liquid (SIL). The results reveal insights into the effects processing conditions have upon possess on full cell battery performance and demonstrate the feasibility of a solid-state cell with monolithic GSE operable at low stack pressures.

2. Experimental Section

2.1. Solid Electrolyte

The GSE selected for this work was the MOS GSE of chemical composition 0.58 Li₂S + 0.315 SiS₂ + 0.105 LiPO₃ (named LiSiPSO).

This GSE was synthesized in 5 g batches by first heat treating lithium sulfide (Li₂S, 99%+ Alfa Aesar) and silicon sulfide (SiS₂, made in-house according to Bayko et al.)^[24] under an inert nitrogen atmosphere (<5 ppm of O₂ and H₂O) at 800 °C for 15 min. The SiS₂ was synthesized via a high-temperature, solid–liquid reaction route using elemental silicon and sulfur. Further details on this process can be found under US Patent 12,071,352 B2.^[24] After heat treatment, lithium metaphosphate (LiPO₃), synthesized in-house via methods described in Wheaton et al.,^[18] was added, and the mixture was milled via a Spex Mill 8100 for 5 min. Finally, the homogenized precursor materials were heated at 850 °C under an inert nitrogen atmosphere for 15 min.^[18] To make ≈1 mm thick GSE disks for full cell assembly, the molten glass was poured into brass cylindrical molds and annealed at 280 °C using methods outlined by Zhao et al.^[25]

2.2. Composite Cathode Synthesis for Optimization

Composite cathode blends were created in a planetary ball mill (Pulverisette 6, Fritsch) in 6 g batches, milled at 150 rpm for 6 h total. Cathode blends with weight ratios 79 wt% LFP + 19 wt% LiSiPSO + 2 wt% carbon were mixed in a zirconia pot with ≈50 g of 10 mm yttria-stabilized zirconia balls as milling media. Four different mixing protocols were used in this work, varying the order in which the components were added during the mixing process as outlined in Figure 1. Method 1 added all three components at the beginning of milling, whereas methods 2, 3, and 4 withheld one component during the first 30 min of milling and introduced

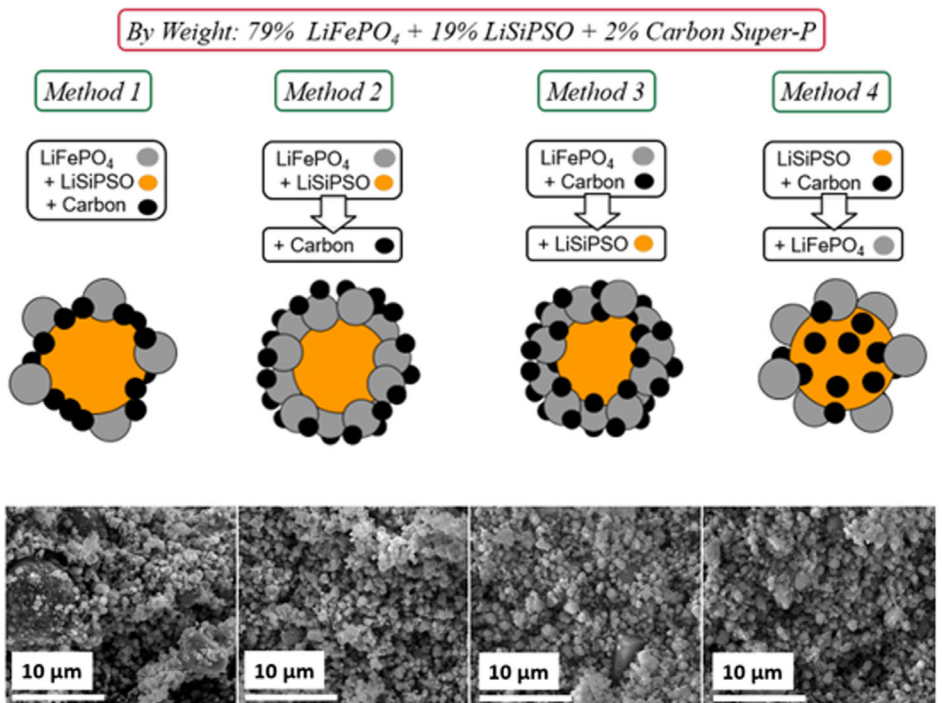


Figure 1. Different mixing protocols and their corresponding SEM images for the composite cathode. Each composite was mixed for 3 h before imaging, varying the mixing order as shown above. The schematic shown above for each protocol is illustrative of the possible microstructure of the composite cathode.

the third component later. Method 2 added the conductive carbon as a second step, method 3 added the LiSiPSO, and method 4 added the LFP after the initial milling step. Samples of the powder were removed at various time intervals throughout mixing to investigate the impact of mixing time on the cathode composite mixtures.

To measure the ionic and electronic conductivities, the powder samples were pressed into 10 mm diameter pellets at 14 MPa using a hydraulic press (YLJ-15, MTI). The pressed pellets were assembled in 2032 coin cells with stainless steel blocking electrodes, as shown in Figure S1, Supporting Information. Electrochemical impedance spectroscopy (EIS) was performed from 10 MHz to 0.1 Hz in a temperature range from -30 to 90 °C on a dielectric impedance spectrometer (Alpha-A, Novocontrol).

2.3. Tape-Cast Composite Cathode Synthesis

After optimization of the mixing of the cathode composite was completed, the composite cathode intended for inclusion in full cells was synthesized via high-energy mixing in a Thinky Mixer ARM-310, followed by tape casting onto an Al foil substrate. All processes were conducted under an inert argon atmosphere (<5 ppm of H₂O and O₂). To begin, 3.5 g batches were prepared using method 4, starting with powdered LiSiPSO mixed in the Thinky Mixer with carbon nanotubes (CN multiwalled, Aldrich) and ≈ 20 g of yttria-stabilized zirconia milling media (YSZ 3 mm spherical, MSE supplies). The materials were mixed at 1000 rpm for a total of 5 min, then LFP (carbon-coated, MTI) was added last per method 4 to the mixing container. This final composite was mixed at 300 rpm for 3 min, then 500 rpm for 3 min, for a dry cathode powder composition of 19 wt% LiSiPSO, 2 wt% carbon nanotubes, and 79 wt% LFP.^[26] A binder solution of 1.89 wt% SBR (30 wt% styrene Aldrich) and 98.11 wt% m-xylene (C₈H₁₀ anhydrous, $\geq 99\%$ Sigma-Aldrich) was created. To prepare the powder composite cathode for tape casting, enough solution was used to create a 50% solids slurry. The binder solution was added in two steps, with half the required volume of SBR solution initially added to 500 mg of powder composite and mixed in the Thinky Mixer at 1500 rpm for 5 min. Then, the remaining half of the solution was added to the mixture and spun in the Thinky Mixer at 1500 rpm for another 5 min. The resulting slurry was tape cast onto aluminum foil under argon atmosphere and allowed to dry under ambient conditions for 24 h. The final composition of the tape-cast composite cathode was 77.4 wt% LFP—18.6 wt% LiSiPSO—2 wt% carbon nanotubes—2 wt% SBR.

2.4. Materials Characterization

2.4.1. Composite Film Scanning Electron Microscopy (SEM)

Characterization of the composite cathode films and powders was accomplished with SEM. SEM observations were performed with an FEI Inspect F50. Samples were transferred into the SEM in a custom airtight sample holder to prevent reaction with the atmosphere. Images were taken in secondary electron mode with

a 12.0 mm working distance. The accelerating voltage was 10.00 kV and the spot size 6.0 nm.

2.4.2. GSE Ionic and Electronic Conductivity

The ionic and electronic conductivities of the LiSiPSO GSE were evaluated with an alpha-A Novocontrol dielectric impedance spectrometer. To measure the ionic conductivity, EIS was performed at frequencies of 10 MHz to 0.1 Hz and at temperature ranges from -30 to 90 °C. To determine the electronic conductivity, the long-term limiting current responses from applying various DC voltages to the GSE sample were obtained. Voltages were applied at 0.05, 0.1, 0.15, 0.2, 0.25, 0.3, 0.4, and 0.5 V for 6 h at each step.

2.4.3. Active Material X-Ray Diffraction

Powder X-ray diffraction was performed on the as-received LFP with a Rigaku SmartLab XRD (Cu K α wavelength of 1.54 Å). Measurements were conducted using a Cu K-Beta filter, a voltage of 40 kV, a current of 44 mA, a scan speed of 1.5° min⁻¹, a step width of 0.01°, and a scanning range of 18°—90°.

2.4.4. Postmortem Raman Spectroscopy

Ex situ Raman spectroscopy was performed on cycled full cell electrolytes and cathodes, both pre- and postmortem, with an inVia 488 nm Renishaw Coherent Laser Raman spectrometer, calibrated to an internal standard silicon reference centered at 520.5 ± 0.4 cm⁻¹. Samples were tested under a 20x objective lens, with a spot size of $\approx(50 \mu\text{m}^2)$, from 200 to 2100 cm⁻¹ with 100 accumulations at 1.25 mW power.

2.5. Full Cell Assembly

After material characterization, the cycling characteristics of the cathode materials were assessed in 2032 coin cells. A 6 mm diameter tape-cast composite cathode film was placed in contact with a polished, 1 μm root mean square (RMS) roughness LiSiPSO disk. A volume of SIL equivalent to 10–20 wt% of the cathode mass ($\approx 0.5 \mu\text{L}$) was placed at the cathode–electrolyte interface. This SIL was synthesized by mixing an equimolar solution of triethylene glycol dimethyl ether (G3, 99% Sigma-Aldrich) and bis(trifluoromethane)sulfonimide lithium salt (LiTFSI, 99.95% metals basis Aldrich), referred to as “LiG3” by Oh et al.^[27] A piece of lithium foil was placed as the anode on the opposite side of the GSE. The electrodes were assembled between two stainless steel current collectors.

2.6. Electrochemical Characterization

For the testing of cell stability, cyclic voltammetry (CV) scanning was performed from 1.8 to 4.2 V versus Li/Li⁺ at a scan rate of 0.025 mV s⁻¹. CV was performed on both full cells and Li asymmetric cells. Asymmetric cells were also constructed in 2032

casings by placing Li foil on one side of the GSE and a stainless-steel electrode on the opposite side and were scanned from -0.1 to 5 V versus Li/Li^+ . EIS over time was performed on a $\text{Li} \mid \text{LiSiPSO} \mid \text{Li}$ symmetric cell to investigate the anode-electrolyte chemical stability. Galvanostatic cycling with potential limitation (GCPL) of the cells was conducted in the voltage range of $2\text{--}4$ V versus Li/Li^+ . Long cycle stability was assessed via GCPL at a rate of C/50 for 100 cycles. The rate capabilities of the cells were tested by GCPL at current rates of C/20, C/10, C/5, C/2, and C/20 for 3 cycles each. The theoretical capacity of the LFP cathode was taken to be 170 mAh g^{-1} . All tests were conducted with a BioLogic VMP-300 Potentiostat.

3. Results and Discussion

3.1. Characterization of the GSE

Before its inclusion in an all-solid-state lithium-ion battery (ASSLIB), the LiSiPSO GSE was characterized to assess its electrochemical behavior. To evaluate ionic conductivity, the equivalent circuit model of the bulk ionic diffusion mechanism within the LiSiPSO glass was assumed to be a parallel combination of a resistor R (DC ionic conductivity) and a constant phase element Q (distributed polarization capacitance).^[18] The temperature-dependent Nyquist plots obtained from EIS were fit at each temperature using this model to obtain the DC Li^+ ionic conductivity of the LiSiPSO GSE at varying temperatures, as shown in Figure 2A. The Li^+ ionic conductivity of the LiPSISO GSE was determined to be $6.32 \times 10^{-4} [\Omega \cdot \text{cm}]^{-1}$ at room temperature with an activation energy of 28.2 kJ mol^{-1} (calculated according

to Kmiec et al.).^[28] This is comparable to the reported conductivities of other GSEs in the $\text{Li}-\text{Si}-\text{P}-\text{S}-\text{O}$ system.^[29] It is further important to note that the LiSiPSO GSE appears to show non-Arrhenius behavior at higher temperatures, an artifact from the testing cell used in the Novocontrol. Testing cells designed for high-frequency EIS experiments would better capture the Arrhenius behavior of the GSE at higher frequencies.

DC polarization was utilized to determine the electronic conductivity of the LiSiPSO GSE. According to an analysis published elsewhere,^[30] the current I within a cell under applied voltage E can be modeled by Equation (1).

$$I = \frac{RTA}{LF} \left\{ \sigma_n [1 - \exp(-u)] + \sigma_p [\exp(u) - 1] \right\} \quad (1)$$

where R is the gas constant, T is the temperature, A is the cross-sectional area of the electrode, L is the electrolyte thickness, F is Faraday's constant, and σ_n and σ_p are the electron and hole conductivities, respectively. u is a dimensionless quantity given in Equation (2).

$$u = \frac{EF}{RT} \quad (2)$$

where E is the potential used in the experiment and the other variables are as in Equation (1).

Rearranging Equation (1) yields Equation (3):

$$\frac{ILF}{RTA[1 - \exp(-u)]} = \sigma_p \exp(u) + \sigma_n \quad (3)$$

A log-log plot of this function yields a slope of $\log(\sigma_p)$ and a y-intercept of $\log(\sigma_n)$. To obtain the electronic conductivity of LiSiPSO, the polished GSE was polarized at various DC voltages from 0.05 to 0.5 V between two stainless steel current collectors. The measured data were fit using Equation (3) and displayed in Figure 2B. The calculated electronic conductivity of LiSiPSO was found to be $2.00 \times 10^{-7} [\Omega \cdot \text{cm}]^{-1}$ as determined from the y-intercept of the plot. Similar MOS glass systems exhibited electronic conductivities over 6 orders of magnitude lower than their ionic conductivities, indicating that the majority of observed current is due to the flow of mobile Li^+ cations.^[31] Comparatively, the measured difference between the ionic and electronic conductivities of the LiSiPSO is less than 3 orders of magnitude. This suggests that the electronic current through the LiSiPSO GSE is much more prominent compared to other MOS GSE systems.

CV of the LiSiPSO GSE was performed in a $\text{Li} \mid \text{LiSiPSO} \mid \text{stainless steel}$ asymmetric cell. As shown in Figure 2C, the electrolyte exhibits no reaction currents outside of the two peaks near 0 V, ascribed to the reversible plating and stripping of lithium. EIS was also performed on a $\text{Li} \mid \text{LiSiPSO} \mid \text{Li}$ symmetric cell to assess its chemical stability in contact with lithium metal. EIS measurements were recorded at regular time intervals, and the subsequent Nyquist plots were fitted to model two mechanisms: the bulk glass resistance and the interfacial resistance between the lithium and GSE. Shown in Figure 2D, the resistance of the bulk GSE remained relatively constant while the interfacial resistance

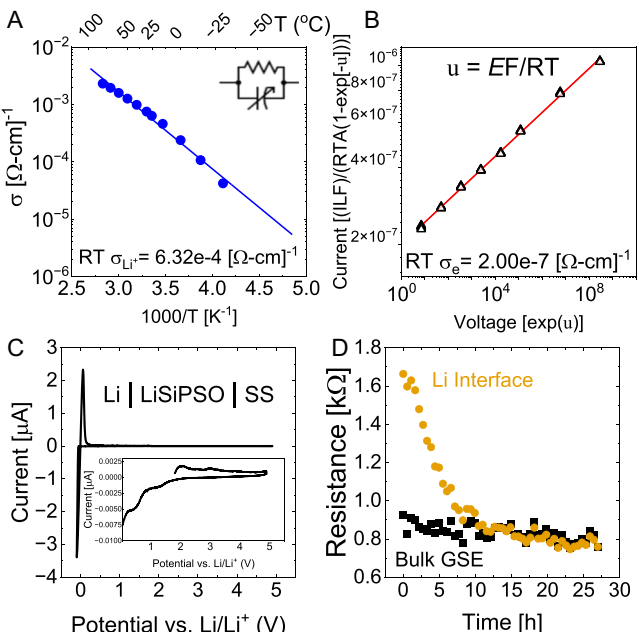


Figure 2. The electrochemical properties of LiSiPSO glass, including its A) ionic conductivity, B) electronic conductivity, C) CV curve versus Li/Li^+ , and D) electrochemical stability in contact with lithium metal over time.

decreased and leveled off over time, indicating the formation of a stable interface between the LiSiPSO glass and lithium metal. It has been suggested that the decrease in interfacial resistance over time may be due to lithium creep filling voids at the interface.^[32,33]

3.2. Optimization of Composite Cathode Processing Conditions

Pressed pellets of composite cathode powder prepared with different mixing methods and mixing times were assessed using EIS at multiple temperatures. The Nyquist plots of all samples shown in Figure 3A contained two semicircles, which were fit using an equivalent circuit of two resistor-constant phase element (RQ) - components in series. The resistance of the larger, high-frequency semicircle decreased with increasing temperature. This pattern aligns with the Arrhenius behavior of ionic conduction; thus, it

was assigned as a marker of the lithium-ion conduction mechanism within the GSE.

The resistance of the smaller, low-frequency semicircle grew with increasing temperature, indicating that the mechanism becomes more resistive as temperature increases. Previous literature reports have assigned this behavior to electron transfer reactions as the charges hop from electrolyte to CAM surfaces in lithium batteries.^[34] Thus, it is proposed that this feature in the Nyquist plot is due to an electron hopping mechanism as the charge transitions at material boundaries within the composite. This feature was assigned to electron transfer and used as a measure of the electronic resistance within the cathode.

The ionic and electronic transport properties of the composite cathode were assessed by fitting the Nyquist plots at multiple temperatures and plotting the resulting conductivities on an inverse temperature plot, shown in Figure 3 C and E. The conductivities measured in Figure 3 C and E were collected after 3 h of milling. For both ionic and electronic conductivity, it was observed that methods 1–3 had generally similar transport properties, whereas the composite cathode prepared via method 4 demonstrated conductivities nearly an order of magnitude higher than the others. In method 4, the GSE and conductive carbon are blended prior to the addition of LFP. It is proposed that these enhanced transport properties are due to the two conducting components becoming well-homogenized (as depicted in Figure 1) within the composite before introducing the active material, thus increasing the number of trijunction points and conduction pathways through the composite cathode.^[35]

To further investigate these trends, DC polarization experiments revealed the Ohmic resistances of composites prepared via different mixing methods (Figure 3F). The results aligned with those obtained from EIS, where composites prepared with methods 1–3 possessed similar slopes (and thus Ohmic resistances) and composites created by method 4 demonstrated a steeper slope. This steeper slope indicates a composite with lower Ohmic resistances, and therefore, higher electronic conductivity. Combined with EIS measurements, these results suggest the conductive carbon network achieves improved electronic transport properties with method 4.

The effect of milling time on the ionic and electronic conductivities were assessed as shown in Figure 3D. It was observed in all methods that increasing the milling time of the mixture reduced its ionic conductivity through the composite. This is thought to be due to a decreased GSE particle size from continued milling. As processing time increases, the particle size of the softer sulfide GSEs decreases, allowing the more mass-abundant LFP to effectively coat the now smaller particles of LiSiPSO, shown schematically in Figure 3B.^[8,36,37] This phenomenon creates isolated “islands” of LiSiPSO within the composite. The conductivity of Li⁺ ions within LFP is about 5 orders of magnitude lower than LiSiPSO, which inhibits lithium transport between the now separated particles of LiSiPSO, lowering the overall ionic conductivity of the composite material.^[38,39] It is important to highlight that this observation does not translate between composites prepared with different mixing methods, i.e., after the same amount of total processing time, composites made with method 3 do not have higher ionic

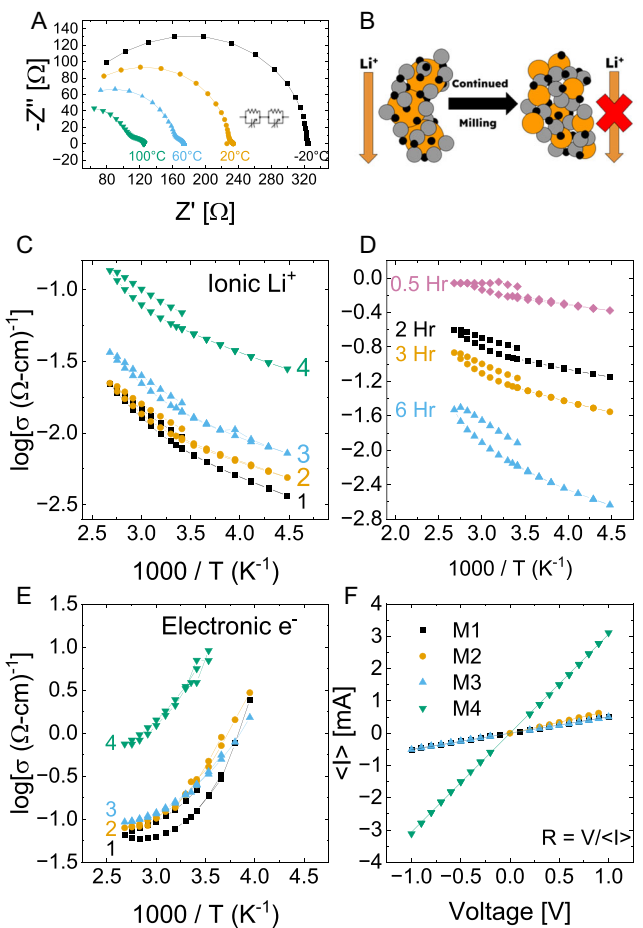


Figure 3. Transport properties of composite cathodes: A) Nyquist plots of temperature dependence of a composite blend. B) Schematic depicting a loss in Li⁺ ion conductivity as decreasing GSE particle size destroys Li⁺ transport pathways. Temperature-dependent C) ionic conductivity and E) electronic conductivity for composite cathodes fabricated via the methods described in Figure 1. D) Temperature-dependent ionic conductivities of a composite cathode milled via method 4 as described in Figure 1. F) DC polarization slopes for composites prepared by methods 1–4.

conductivities than those made with method 4, despite the GSE undergoing less milling in the former.

3.3. Full Cell Cycling

Proceeding on the results from the optimization work, a cathode composite produced using method 4 was selected to be tape-cast and utilized as the cathode in the assessment of ASSLIB full cells consisting of a composite cathode and a thick Li foil anode. Rate capability testing was performed to assess the transport properties of the optimized composite cathodes. A full cell was charged and discharged at rates of C/20 to C/2 for three cycles each, as shown in Figure 4A. An increase in capacity is observed as the cell continued to cycle, perhaps due to continuously improved wetting in the electrodes from the SIL. No substantial loss in specific capacity was witnessed until a rate of C/2 was used, indicating that both the GSE and composite cathode can perform well at increasingly large current densities. It is proposed that the cell is in part capable of these increased power outputs because of the cathode's minimal internal resistances due to its optimization for transport properties.

The CV of a full cell displayed two primary peaks with a mid-point of 3.4 V, as shown in Figure 4B. The charging peak has a peak current of ≈ 0.059 mA, whereas the discharging peak

is ≈ -0.033 mA. Stepwise integration of the CV curve estimates a coulombic charge/discharge ratio of 1.03 (i.e., 1.03 Li⁺ was deintercalated for every intercalated Li⁺ on the subsequent reverse sweep). This loss in charge from the anodic to cathodic sweep suggests that the charge and discharge processes within the full cell are not completely reversible.^[40]

To investigate this irreversibility and test long-term cell performance, full cells were cycled at a rate of C/50 for 100 cycles, as shown in Figure 4C. The cells began with an initial specific capacity ≈ 100 mAh g⁻¹ (compared to LFP's theoretical 170 mAh g⁻¹ and based on the mass loading of LFP in the cathode) and a coulombic efficiency of about 99%.^[41] The poor initial capacity relative to the expected theoretical is likely due to isolated islands of LFP CAM. The charge–discharge curves in Figure 4D show an increasing overpotential and unstable charge–discharge behavior, suggesting an increasing charge transfer resistance and side reactions at the composite cathode.^[42] After 100 cycles, the capacity of the cell faded by over 60% and the coulombic efficiency grew increasingly erratic. This rise-and-fall behavior is indicative of a growing cell instability and fading capacity.^[43]

Table 1 shows the performance of this cell configuration alongside other ASSLIBs that utilize sulfide SSEs with an LFP cathode. While not meeting the performance metrics (discharge

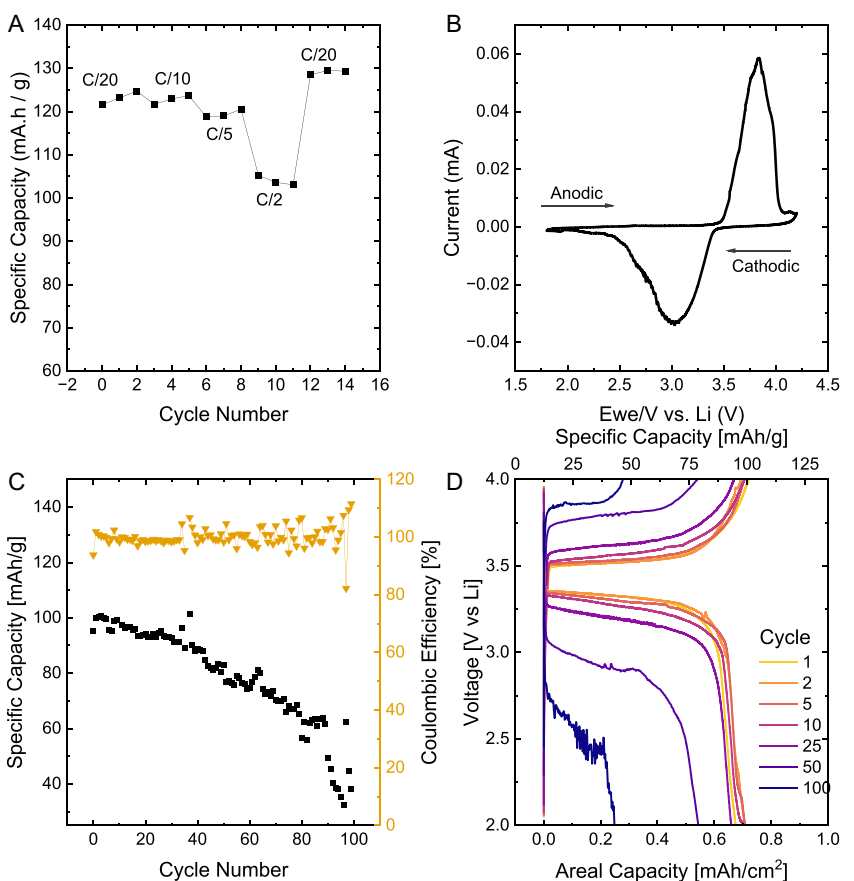


Figure 4. Testing of full cells constructed from lithium metal anode, LiSiPSO GSE, and optimized composite cathode. Rate capability A) was performed from C/20 to C/2. CV B) displays two oxidation-reduction peaks and long-term cycling conducted over 100 cycles C) indicates a growing cell instability seen in the D) charge–discharge curves.

Table 1. Comparison of sulfide SE + LFP based ASSLIBs.

Sample	Solid Electrolyte	Conductive Additive [wt%]	Stack Pressure [MPa]	Discharge Capacity [mAh g^{-1}]		References
				Initial	After Cycling	
1	Powder $\text{Li}_6\text{PS}_5\text{Cl}$	Vapor-grown Carbon Fiber (VGCF) (5)	Not Reported	141 (C/10)	128 (1000)	[50]
2	Powder 80Li ₂ S-20P ₂ S ₅	Acetylene Black (AC) (6)	Not Reported	110 (C/55)	40 (10)	[51]
3	Monolithic LiSiPSO	Carbon Nanotubes (2)	<1 Mpa	101 (C/20)	38 (100)	This Work

capacity near theoretical, long cycle life) of ASSLIBs that employ argyrodite $\text{Li}_6\text{PS}_5\text{Cl}$, the cells reported herein are approaching this echelon of performance whilst overcoming the need for high-pressure compaction or large stack pressures.

3.4. Postmortem Analysis

To investigate the cause of the capacity fade seen in Figure 4C, Raman spectroscopy was performed on the full cells after cycling. Both the LiSiPSO GSE A) and composite cathode film B) were scanned pre- and postmortem and the Raman spectra are given in Figure 5. Within the GSE, prominent Raman peaks were observed at 260 cm^{-1} and assigned to bending modes of tetrahedral PS_4^{3-} short range order (SRO) species,^[44,45] 386 cm^{-1} assigned to symmetric stretching modes of $\text{P}_2\text{S}_6^{4-}$ SRO species,^[25,44] 421 cm^{-1} assigned to symmetric stretching modes of PS_4^{3-} SRO species,^[46,47] and 559 cm^{-1} assigned to symmetric stretching modes of $\text{Si}_2\text{S}_6^{4-}$ SRO species.^[44,46] The Raman spectra of the GSE exhibited no significant changes due to cycling, suggesting the bulk GSE remains chemically unmodified throughout the charging/discharging process.

Conversely, changes in the spectrum of the cathode film were observed postmortem. Two distinct peaks are seen near a Raman shift of 1500 cm^{-1} , commonly referred to as the carbon doublet. There exists a notable increase in the magnitude of the peak at 1440 cm^{-1} postcycling.^[48] This peak is often ascribed to defects and disorder within the carbon structure, so it is likely that the mechanical structure of the composite cathode deteriorates as

cycling continues.^[48] Thus, it is proposed that continued cycling degrades the structure of the carbon network within the composite, reducing the cell's available capacity over time. Combined with the interfacial instability commonly seen between LFP and sulfide-based electrolytes, these mechanisms help explain the deterioration of performance seen in Figure 4C.^[49]

4. Conclusions

In order to better understand the effects of processing conditions on cathodes for ASSLIBs, a series of composite cathode blends was tested in conjunction with the novel LiSiPSO GSE. The processing conditions of this cathode blend were optimized for ionic and electronic transport throughout the composite. It was found that mixing the ionic and electronic conducting materials first (method 4) before adding CAM increased transport properties. It is suggested that this mixing order increases the number of conduction pathways and trijunction points. Furthermore, shorter milling times allowed for higher electronic and ionic conductivities. It is postulated that longer milling times destroy conduction pathways and reduce the composite cathode's conductivity. Composite cathodes synthesized via 1 h of milling using method 4 were selected for usage in conjunction with bulk pieces of LiSiPSO to fabricate full cell LIBs. Cycling of these novel cells showed good specific capacities and good coulombic efficiencies. Long-term cycling, CV, and postmortem Raman spectroscopy all indicate a growing cell instability and irreversible reaction that

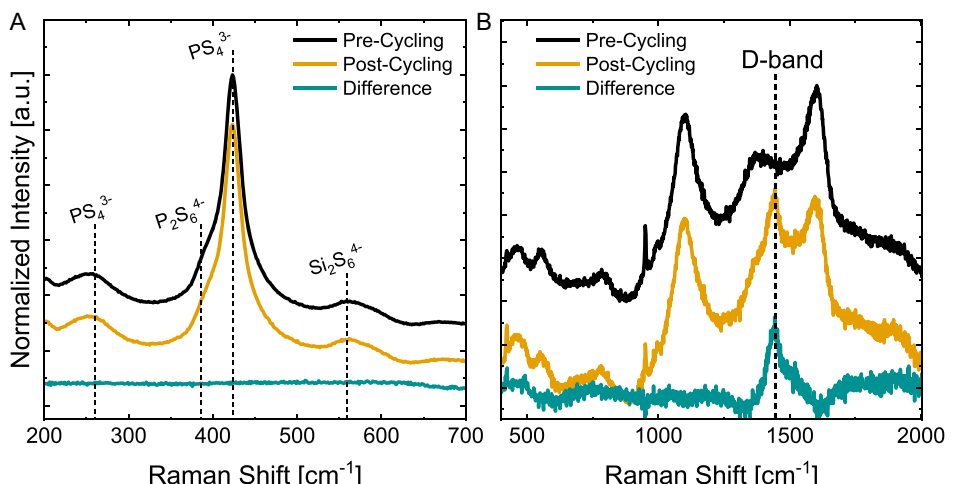


Figure 5. Pre- and postmortem Raman spectroscopy of Li-anode full cells on the bulk GSE A) and composite cathode film B).

warrant further investigation to yield even higher performance LIBs. This work provides important insights for cathode processing techniques in solid-state batteries.

Acknowledgments

Funding for this work was provided by the NASA EPSCoR program through contract number 90NNSSC20M0219, by the Vehicle Technology Office of the EERE office of the Department of Energy through contract number DE-EE0008852, and by the National Science Foundation Division of Materials Research Ceramics Program through awards 1936913 and 2425024.

Conflict of Interest

The authors declare no conflict of interest.

Author Contributions

Will Fettkether: Conceptualization (equal); data curation (lead); formal analysis (lead); investigation (lead); methodology (equal); project administration (lead); (software) (lead); validation (lead); (writing)—original draft (lead); (writing)—review & editing (lead); **Jacob Wheaton:** formal analysis (supporting); investigation (supporting); supervision (equal); validation (equal); (writing)—original draft (supporting); (writing)—review & editing: (equal); **Nicholas H. Bashian:** conceptualization (equal); data curation (supporting); formal analysis (supporting); investigation (supporting); methodology (equal); project administration (supporting); supervision (equal); (writing)—review & editing (equal); **Steve W. Martin:** funding acquisition (lead); resources (lead); supervision (lead); (writing)—review & editing (equal).

Data Availability Statement

The data that support the findings of this study are available from the corresponding author upon reasonable request.

Keywords: glassy solid electrolytes · methods · oxysulfide · processing · solid-state batteries

- [1] J. M. Tarascon, M. Armand, *Nature* **2001**, *414*, 359.
- [2] Z. Yang, J. Zhang, M. C. W. Kintner-Meyer, X. Lu, D. Choi, J. P. Lemmon, J. Liu, *Chem. Rev.*, **2011**, *111*, 3577.
- [3] N. Chawla, N. Bharti, S. Singh, *Batteries* **2019**, *5*, 19.
- [4] Y. Chen, Y. Kang, Y. Zhao, L. Wang, J. Liu, Y. Li, Z. Liang, X. He, X. Li, N. Tavajohi, et al., *J. Energy Chem.* **2021**, *59*, 83.
- [5] C. H. Chen, S. Xie, E. Sperling, A. S. Yang, G. Henriksen, K. Amine, *Solid State Ion.* **2004**, *167*, 263.
- [6] R. C. Xu, X. H. Xia, S. Z. Zhang, D. Xie, X. L. Wang, J. P. Tu, *Electrochim. Acta* **2018**, *284*, 177.
- [7] J. Wu, L. Yuan, W. Zhang, Z. Li, X. Xie, Y. Huang, *Energy Environ. Sci.* **2021**, *14*, 12.
- [8] F. Han, A. S. Westover, J. Yue, X. Fan, F. Wang, M. Chi, D. N. Leonard, N. J. Dudney, H. Wang, C. Wang, *Nat. Energy* **2019**, *4*, 187.
- [9] Y. Xiao, Y. Wang, S.-H. Bo, J. C. Kim, L. J. Miara, G. Ceder, *Nat. Rev. Mater.* **2020**, *5*, 105.
- [10] M. Tatsumisago, A. Hayashi, *Solid State Ionics* **2012**, *225*, 342.
- [11] J. Sastre, M. H. Futscher, L. Pompizi, A. Aribia, A. Priebe, J. Overbeck, M. Stiefel, A. N. Tiwari, Y. E. Romanyuk, *Commun. Mater.* **2021**, *2*, 76.
- [12] R. Zhao, G. Hu, S. Kmiec, J. Wheaton, V. M. Torres Iii, S. W. Martin, *Batteries Supercaps* **2022**, *5*, e202100356.
- [13] R. Zhao, G. Hu, S. Kmiec, R. Gebhardt, A. Whale, J. Wheaton, S. W. Martin, *ACS Appl. Mater. Interfaces* **2021**, *13*, 26841.
- [14] M. Tatsumisago, A. Hayashi, *Chalcogenide Glasses*, X. Zhang, Adam J.-L. Woodhead Publishing: London, UK, **2014**, 632–654.
- [15] T. Minami, A. Hayashi, M. Tatsumisago, *Solid State Ionics* **2006**, *177*, 2715.
- [16] J. Schnell, T. Günther, T. Knoche, C. Vieider, L. Köhler, A. Just, M. Keller, S. Passerini, G. Reinhart, *J. Power Sources* **2018**, *382*, 160.
- [17] A. C. Luntz, J. Voss, K. Reuter, *J. Phys. Chem. Lett.* **2015**, *6*, 4599.
- [18] J. Wheaton, S. Kmiec, D. Schuler, C. Sorensen, S. W. Martin, *Acs Appl. Energy Mater.* **2021**, *4*, 10835.
- [19] M. Olson, J. Wheaton, M. Okkema, N. Oldham, S. W. Martin, *Acs Appl. Energy Mater.* **2023**, *6*, 5842.
- [20] K. G. Naik, M. K. Jangid, B. S. Vishnugop, N. P. Dasgupta, P. P. Mukherjee, *Adv. Energy Mater.* **2025**, *15*, 2403360.
- [21] D. Hlushkou, A. E. Reising, N. Kaiser, S. Spannenberger, S. Schlabach, Y. Kato, B. Roling, U. Tallarek, *J. Power Sources* **2018**, *396*, 363.
- [22] A. K. Padhi, K. S. Nanjundaswamy, J. B. Goodenough, *J. Electrochem. Soc.* **1997**, *144*, 1188.
- [23] K. Zaghib, A. Guerfi, P. Hovington, A. Vijh, M. Trudeau, A. Mauger, J. B. Goodenough, C. M. Julien, *J. Power Sources* **2013**, *232*, 357.
- [24] D. P. Bayko, S. Kmiec, S. W. Martin, *Method of Making High Quality Silicon Sulfide*. US Patent 12,071,352, August 27, 1924.
- [25] R. Zhao, S. Kmiec, G. Hu, S. W. Martin, *ACS Appl. Mater. Interfaces* **2020**, *12*, 2327.
- [26] D. Y. Oh, Y. J. Nam, K. H. Park, S. H. Jung, S.-J. Cho, Y. K. Kim, Y.-G. Lee, S.-Y. Lee, Y. S. Jung, *Adv. Energy Mater.* **2015**, *5*, 1500865.
- [27] S. Kmiec, M. Olson, M. Kenney, S. W. Martin, *Chem. Mater.* **2022**, *34*, 9479.
- [28] S. Kondo, K. Takada, Y. Yamamura, *Solid State Ionics* **1992**, *53*, 1183.
- [29] J. B. Wagner, C. Wagner, *J. Chem. Phys.* **1957**, *26*, 1597.
- [30] T. Ohtomo, F. Mizuno, A. Hayashi, K. Tadanaga, M. Tatsumisago, *J. Power Sources* **2005**, *146*, 715.
- [31] W. S. LePage, *J. Electrochem. Soc.* **2019**, *166*.
- [32] M. J. Wang, R. Choudhury, J. Sakamoto, *Joule* **2019**, *3*, 2165.
- [33] S. Kazemianbnavi, P. Dutta, S. Banerjee, *Phys. Chem. Chem. Phys.* **2015**, *17*, 11740.
- [34] S. Noh, W. T. Nichols, M. Cho, D. Shin, *J. Electroceram.* **2018**, *40*, 293.
- [35] T. Rouxel, S. Yoshida, *J. Am. Ceram. Soc.* **2017**, *100*, 4374.
- [36] J. Wolfenstine, H. Jo, Y.-H. Cho, I. N. David, P. Askeland, E. D. Case, H. Kim, H. Choe, J. Sakamoto, *Mater. Lett.* **2013**, *96*, 117.
- [37] J. Molenda, A. Kulka, A. Milewska, W. Zająć, K. S. Świerczek, *Materials* **2013**, *6*, 1656.
- [38] C. Wang, J. Hong, *Electrochem. Solid-State Lett.* **2007**, *10*, A65.
- [39] D. Y. W. Yu, C. Fietzek, W. Weydanz, K. Donoue, T. Inoue, H. Kurokawa, S. Fujitani, *J. Electrochem. Soc.* **2007**, *154*, A253.
- [40] B. Lung-Hao Hu, F.-Y. Wu, C.-T. Lin, A. N. Khlobystov, L.-J. Li, *Nat. Commun.* **2013**, *4*, 1687.
- [41] A. Cronk, Y.-T. Chen, G. Deysher, S.-Y. Ham, H. Yang, P. Ridley, B. Sayahpour, L. H. B. Nguyen, J. A. S. Oh, J. Jang, et al., *Acs Energy Lett.* **2023**, *8*, 827.
- [42] F. Yang, D. Wang, Y. Zhao, K.-L. Tsui, S. J. Bae, *Energy* **2018**, *145*, 486.
- [43] A. Kaniyoor, S. Ramaprabhu, *AIP Adv.* **2012**, *2*, 032183.
- [44] T. Kim, K. Kim, S. Lee, G. Song, M. S. Jung, K. T. Lee, *Chem. Mater.* **2022**, *34*, 9159.
- [45] V. Torres III, S. W. Martin, *Inorg. Chem.* **2023**, *62*, 8271.
- [46] T. Ohtomo, F. Mizuno, A. Hayashi, K. Tadanaga, M. Tatsumisago, *Solid State Ionics* **2005**, *176*, 2349.
- [47] C. Bischoff, K. Schuller, M. Haynes, S. W. Martin, *J. Non Cryst. Solids* **2012**, *358*, 3216.

- [48] K. Sun, C. Cao, D. Zhao, X. Tong, S.-M. Bak, Y. Du, F. Wang, D. A. Steingart, *J. Phys. Chem. C* **2023**, *127*, 19396.
- [49] K. Ohara, A. Mitsui, M. Mori, Y. Onodera, S. Shiotani, Y. Koyama, Y. Orikasa, M. Murakami, K. Shimoda, K. Mori, et al., *Sci. Rep.* **2016**, *6*, 21302.
- [50] A. Sakuda, H. Kitaura, A. Hayashi, M. Tatsumisago, Y. Hosoda, T. Nagakane, A. A.-S.-S. Sakamoto, *Chem. Lett.* **2012**, *41*, 260.
- [51] Y. J. Nam, D. Y. Oh, S. H. Jung, Y. S. Jung, *J. Power Sources* **2018**, *375*, 93.

Manuscript received: June 10, 2025

Revised manuscript received: August 22, 2025

Version of record online:
